





# Tuning the activities of cuprous oxide nanostructures via the oxide-metal interaction

Wugen Huang<sup>1,2,7</sup>, Qingfei Liu<sup>1,2,6,7</sup>, Zhiwen Zhou<sup>1,2</sup>, Yangsheng Li<sup>1,2</sup>, Yunjian Ling<sup>1,2</sup>, Yong Wang<sup>3</sup>, Yunchuan Tu<sup>1</sup>, Beibei Wang<sup></sup><sup>4</sup>, Xiaohong Zhou<sup>4</sup>, Dehui Deng<sup>1</sup>, Bo Yang<sup></sup><sup>4</sup>, Yong Yang<sup></sup><sup>4</sup>, Zhi Liu<sup>4,5</sup>, Xinhe Bao<sup>1</sup> & Fan Yang<sup></sup><sup>1,4</sup>✉

Despite tremendous importance in catalysis, the design of oxide-metal interface has been hampered by the limited understanding of the nature of interfacial sites and the oxide-metal interaction (OMI). Through construction of well-defined Cu<sub>2</sub>O/Pt, Cu<sub>2</sub>O/Ag and Cu<sub>2</sub>O/Au interfaces, we find that Cu<sub>2</sub>O nanostructures (NSs) on Pt exhibit much lower thermal stability than on Ag and Au, although they show the same structure. The activities of these interfaces are compared for CO oxidation and follow the order of Cu<sub>2</sub>O/Pt > Cu<sub>2</sub>O/Au > Cu<sub>2</sub>O/Ag. OMI is found to determine the activity and stability of supported Cu<sub>2</sub>O NSs, which could be described by the formation energy of interfacial oxygen vacancy. Further, electronic interaction between Cu<sup>+</sup> and metal substrates is found center to OMI, where the *d* band center could be used as a key descriptor. Our study provides insight for OMI and for the development of Cu-based catalysts for low temperature oxidation reactions.

<sup>1</sup>State Key Laboratory of Catalysis, Dalian Institute of Chemical Physics, Chinese Academy of Sciences, 116023 Dalian, China. <sup>2</sup>University of Chinese Academy of Sciences, 100049 Beijing, China. <sup>3</sup>State Key Laboratory of Physical Chemistry of Solid Surfaces, iChEM, College of Chemistry and Chemical Engineering, Xiamen University, 361005 Xiamen, China. <sup>4</sup>School of Physical Science and Technology, ShanghaiTech University, 201210 Shanghai, China. <sup>5</sup>State Key Laboratory of Functional Materials for Informatics, Shanghai Institute of Microsystem and Information Technology, Chinese Academy of Sciences, 200050 Shanghai, China. <sup>6</sup>Present address: College of Chemistry and Chemical Engineering, Chongqing University, 400044 Chongqing, China. <sup>7</sup>These authors contributed equally: Wugen Huang, Qingfei Liu. ✉email: [fyang@dicp.ac.cn](mailto:fyang@dicp.ac.cn)

Metal alloy catalysts<sup>1</sup> are widely used for technical applications in chemical industry<sup>2,3</sup>, environmental remediation<sup>4</sup>, and energy conversion<sup>5</sup>. These alloy catalysts usually consist of a precious metal component and a cheap metal component, the latter of which would segregate to the surface under oxidative conditions to form a self-limited oxide layer<sup>6</sup>. Such phenomena have been utilized recently for the controlled synthesis of two-dimensional (2D) oxide layer<sup>7</sup>. In catalysis, studies on the formation of interfacial oxide layer on precious metal surfaces could be traced back to the discovery of strong metal support interaction (SMSI)<sup>8</sup> and nowadays increasingly found for metal alloy catalysts in catalytic oxidation reactions center for industrial catalysis. Despite tremendous interest, atomic understanding on the catalytic nature of these oxide layers remains a long-standing challenge because interfacial sites are minority surface sites and difficult to access. Nevertheless, the unique catalytic properties of the oxide–metal interface<sup>9–13</sup> have now been recognized, although how oxide–metal interaction (OMI) tunes the properties of interfacial sites remains largely unknown.

The interface between cuprous oxide and metal has been a system of particular catalytic interest, but difficult to study owing to the dynamic nature of copper centers<sup>14</sup>, i.e., their valence states and coordination numbers vary with the reaction environment. Coordinatively unsaturated (CUS) metal cations have often been found as active sites for catalytic reactions. For instance, CUS Cu<sup>+</sup> centers are active sites for the oxidation of ethylbenzene to acetophenone<sup>15</sup>. Owing to the stability and activity requirements of technological applications, stabilizing CUS centers on precious metal surfaces has been developed as an effective strategy, as demonstrated by interface-confined ferrous centers for the preferential oxidation reaction<sup>12</sup>. Indeed, the alloy between Cu and group VIII metals<sup>16–20</sup>, especially Pt, are excellent catalysts for oxygen reduction reaction, whereas alloy catalysts consisting of copper and group IB metals<sup>21–23</sup> exhibit remarkable performances for the selective oxidation of hydrocarbons. Meanwhile, the formation of a copper oxide–metal interface has been generally observed on PtCu<sup>24</sup>, AuCu<sup>25</sup>, and AgCu<sup>26</sup> during oxidation reactions even under mild conditions. Undoubtedly, an atomic-scale understanding on the catalytic properties of the Cu<sub>2</sub>O–metal (Cu<sub>2</sub>O–M) interface is essential to the design and improvement of Cu-based alloy catalysts for oxidation reactions.

Here, we synthesize well-defined Cu<sub>2</sub>O NSs on Pt(111), Au(111), and Ag(111), and study their interfacial structures and chemistry using the combination of low-temperature scanning tunneling microscopy (LT-STM), near-ambient-pressure STM (NAP-STM), X-ray photoelectron spectroscopy (XPS), and density functional theory (DFT) calculations. The atomic structures of interfacial sites are identified unambiguously with element-specific STM (ES-STM) images. Despite the same interfacial site structure, the activities of the Cu<sub>2</sub>O/Pt, Cu<sub>2</sub>O/Au, and Cu<sub>2</sub>O/Ag interfaces for CO oxidation are found strongly dependent on OMI, where Cu<sub>2</sub>O/Pt and Cu<sub>2</sub>O/Au are found to exhibit a reversible structural dynamics during the redox reaction at low temperatures. Our study unravels key factor in determining OMI, and subsequently the activity and stability of supported Cu<sub>2</sub>O NSs, which furthers our understanding on OMI and provides insight for the development of metal alloy catalysts.

## Results

**Atomic structures of Cu<sub>2</sub>O NSs on metal substrates.** Cu<sub>2</sub>O NSs were synthesized on Pt(111), Au(111), and Ag(111) using the method described in the experimental section and display various sizes with monolayer (ML) thickness (Supplementary Fig. 1). Their atomic structures, both on the surface and at the step edge,

could be clearly identified by ES-STM images<sup>27–29</sup> (Fig. 1). In the Cu-mode STM image, Cu atoms were resolved as bright dots and exhibit a kagome (trihexagonal stacking) lattice. In the O-mode STM image, O atoms were imaged as protrusions and display a hexagonal lattice. Combining the Cu-mode and O-mode STM images, these Cu<sub>2</sub>O NSs are found to display a Cu<sub>2</sub>O(111)-like structure, which exhibits the honeycomb lattice of Cu<sub>2</sub>O(111) (Fig. 1j), but does not have dangling Cu atoms at the center of honeycomb, owing to their instability on metal substrates (Fig. 1k). The honeycomb lattice of these Cu<sub>2</sub>O NSs on Pt(111), Au(111), or Ag(111) displays the unit cell length (~ 6.0 Å) same as that of Cu<sub>2</sub>O(111). But, due to the missing of dangling Cu atoms, supported Cu<sub>2</sub>O NSs exhibit the stoichiometry of Cu<sub>3</sub>O<sub>2</sub>, which has been generally observed for ML Cu<sub>2</sub>O NSs grown on metal substrates<sup>27,30</sup>.

In the surface lattice of Cu<sub>2</sub>O NSs, 5–7 topological defects<sup>30</sup> could also be observed, especially for Cu<sub>2</sub>O NSs supported on Ag(111) (Fig. 1g). These 5–7 topological defects were formed via the Stone-Wales type transformation of the Cu<sub>3</sub>O<sub>2</sub> honeycomb lattice, which has been discussed previously<sup>30</sup>. After the annealing in ultrahigh vacuum (UHV), the step edges of Cu<sub>2</sub>O NSs on Pt(111), Au(111), and Ag(111) also exhibited dominantly the same O-terminated zig-zag structure, as identified by ES-STM images (Fig. 1 and Supplementary Fig. 2). On Au(111), we have shown that the O-terminated zig-zag step is thermodynamically favored<sup>27</sup> and would become the dominant step structure after the annealing at 600 K, which also appears to be the case for Pt(111) and Ag(111).

Although Cu<sub>2</sub>O NSs on Pt(111), Au(111), and Ag(111) show the same surface and step structures, their stability was found to be influenced by OMI<sup>31</sup>. We found that Cu<sub>2</sub>O NSs on Pt(111) would start to decompose at ~470 K and decompose completely at ~630 K (Supplementary Fig. 3a, b), which was accompanied by the diffusion of Cu atoms into the bulk. Since the desorption of atomic oxygen atoms on Pt(111) would start at above 500 K<sup>32</sup>, the low stability of Cu<sub>2</sub>O NSs on Pt(111) seems to suggest that these Cu<sub>2</sub>O NSs could be highly active for CO oxidation. In contrast, Cu<sub>2</sub>O NSs appeared stable on Au(111) and Ag(111) after the annealing at 600 K (Supplementary Fig. 3c, e) although they would start to coalesce and form larger islands after the annealing at 700 K (Supplementary Fig. 3d, f). Thus, the difference in thermal stability of supported Cu<sub>2</sub>O NSs indicates that interfacial interaction could play a key role in determining their stability and reactivity.

**CO adsorption and reaction at the Cu<sub>2</sub>O–metal interface.** The adsorption and reaction of CO were then compared for Cu<sub>2</sub>O NSs on Pt(111), Au(111), and Ag(111). When the Cu<sub>2</sub>O/Pt(111) surface was exposed to CO at 78 K, CO adsorbed randomly on Pt(111) and the surface of Cu<sub>2</sub>O NSs remained clean, indicating a weak interaction between CO and Cu<sub>2</sub>O (Fig. 2a and Supplementary Fig. 4). Continuous CO exposure at 78 K could cause the appearance of CO molecules on the surface domains of Cu<sub>2</sub>O (Fig. 2b). But, analysis of high-resolution STM image showed that these CO molecules were located dominantly on Pt sites exposed at the center of the hexagonal Cu<sub>2</sub>O rings (Supplementary Fig. 5), owing to the much stronger chemisorption of CO on Pt<sup>33</sup>. The large holes of the Cu<sub>2</sub>O rings allow for CO adsorption on Pt sites even when Pt(111) is fully covered by Cu<sub>2</sub>O.

The CO-covered surface of Cu<sub>2</sub>O/Pt(111) was then annealed to 300 K in UHV. Figure 2c showed the reduction of Cu<sub>2</sub>O NSs by CO, starting from both the surface terrace of Cu<sub>2</sub>O and the step edges of Cu<sub>2</sub>O. From the development of reaction front, the reaction rate of Cu<sub>2</sub>O reduction from the step edges of Cu<sub>2</sub>O was found to be faster (~1.3 times) than that on the surface terrace of

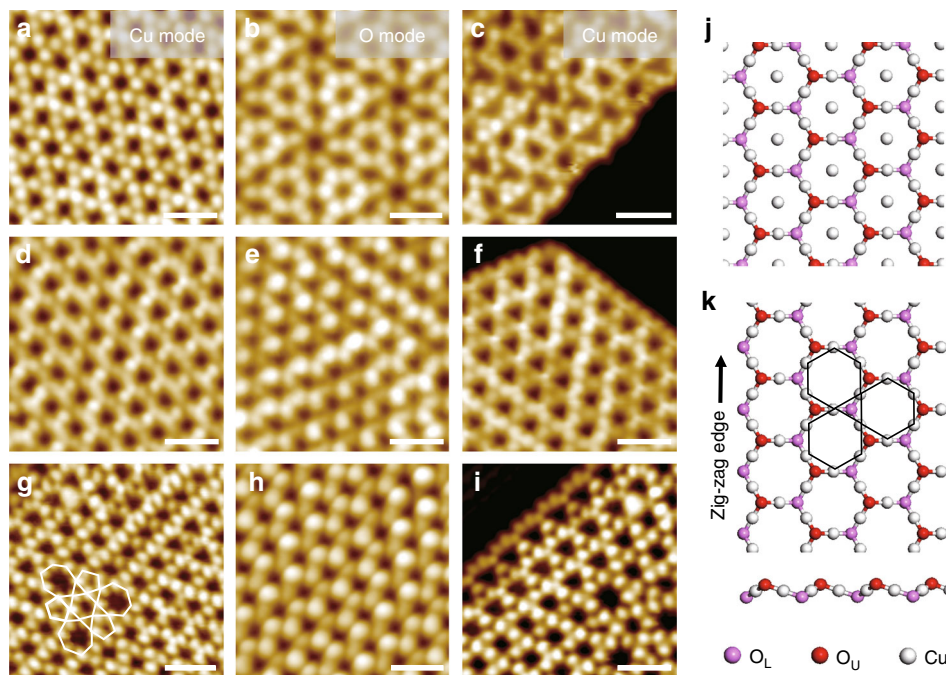


**Fig. 1** Element-specific STM images of  $\text{Cu}_2\text{O}$  NSs grown on metal substrates. **a–i** STM images of **a–c**  $\text{Cu}_2\text{O}/\text{Pt}(111)$ , **d–f**  $\text{Cu}_2\text{O}/\text{Au}(111)$ , and **g–i**  $\text{Cu}_2\text{O}/\text{Ag}(111)$ . The surface structures of  $\text{Cu}_2\text{O}$  NSs are displayed in the left column (Cu-mode: Cu atoms were resolved as bright dots) and the middle column (O mode: O atoms were resolved as bright protrusions) of STM images. The edge structures of  $\text{Cu}_2\text{O}$  NSs are displayed in the right column (Cu-mode) of STM images showing zig-zag step structure with oxygen termination. 5–7 defects in  $\text{Cu}_2\text{O}$  NS on  $\text{Ag}(111)$  are marked by white lines in **g**. **j** The structural model of  $\text{Cu}_2\text{O}(111)$  surface. **k** The structural model of supported  $\text{Cu}_2\text{O}$  NSs in **a–i**.  $\text{O}_U$  and  $\text{O}_L$  represent the upper O and lower O, respectively. All  $\text{Cu}_2\text{O}$  NSs exhibit the hexagonal lattice of  $\text{Cu}_2\text{O}(111)$  without dangling Cu atoms at the center of honeycomb and with an oxygen-terminated zig-zag edge. Scanning parameters: **a**  $V_s = -0.4$  V,  $I = 1.1$  nA; **b**  $V_s = -0.2$  V,  $I = 1.4$  nA; **c**  $V_s = -0.05$  V,  $I = 3.0$  nA; **d**  $V_s = -0.2$  V,  $I = 1.5$  nA; **e**  $V_s = -1.15$  V,  $I = 1.2$  nA; **f**  $V_s = -0.1$  V,  $I = 2.1$  nA; **g**  $V_s = -0.32$  V,  $I = 0.79$  nA; **h**  $V_s = 0.5$  V,  $I = 0.1$  nA; **i**  $V_s = -0.32$  V,  $I = 0.79$  nA. Scale bars: 1 nm for all images.

$\text{Cu}_2\text{O}$  (Supplementary Fig. 6). The faster reduction rate along the steps of  $\text{Cu}_2\text{O}$  could be attributed to the lower coordination numbers of O atoms at step edges. Nonetheless, CO oxidation at both the step edge and the surface terrace of  $\text{Cu}_2\text{O}$  occurred via an interfacial dual-site reaction mechanism, i.e., CO adsorbed on Pt sites to react with neighboring lattice oxygen in  $\text{Cu}_2\text{O}$ .

Consistently, when the  $\text{Cu}_2\text{O}/\text{Pt}(111)$  surface was exposed to CO at 300 K, the reduction of  $\text{Cu}_2\text{O}$  could start right upon the exposure to  $5 \times 10^{-8}$  mbar CO and the exposure to  $1 \times 10^{-7}$  mbar CO for 5 min at 300 K could lead to the complete decomposition of  $\text{Cu}_2\text{O}$  layer into metallic Cu atoms or triangular  $\text{Cu}_3\text{O}_x$  clusters (Fig. 2d–e). These  $\text{Cu}_3\text{O}_x$  clusters sit on a metallic layer with its apparent height ( $\sim 2$  Å, Supplementary Fig. 7) approximating the step height of  $\text{Cu}(111)$ . The metallic layer exhibited a hexagonal lattice with a non-uniform lattice spacing ( $\sim 5$  Å), which is approximately twice that of  $\text{Cu}(111)$  and indicating the formation of a  $\text{PtCu}_3$  alloy (Supplementary Fig. 7d). The exothermic reaction of CO oxidation could facilitate the alloying between Cu and Pt since the formation of  $\text{PtCu}_3$  is a thermodynamically favored process<sup>34</sup>. Accordingly, XPS O 1s spectra (Fig. 2f) showed that only  $\sim 10\%$  of  $\text{Cu}_2\text{O}$  was left when 0.6 ML  $\text{Cu}_2\text{O}/\text{Pt}(111)$  was exposed to CO at 300 K. CO exposure also led to the adsorption of CO on bridge and top sites of Pt (111), as shown in the O 1s spectra<sup>35</sup>. In comparison, when the Pt (111) surface is fully covered by  $\text{Cu}_2\text{O}$ , the reduction of the  $\text{Cu}_2\text{O}$  layer requires a higher CO pressure at  $5 \times 10^{-6}$  mbar (Supplementary Fig. 8). The major problem that prevents Pt group metals from catalyzing low temperature CO oxidation is the strong chemisorption (poisoning) of CO blocks surface sites for the adsorption and activation of  $\text{O}_2$ . The superior activity of supported  $\text{Cu}_2\text{O}$  NSs demonstrated above showed that such

problem could be annihilated by the formation of a  $\text{Cu}_2\text{O}/\text{Pt}$  interface.

In comparison, when the  $\text{Cu}_2\text{O}/\text{Au}(111)$  surface was exposed to CO at 78 K (Fig. 3a, b), no adsorption of CO molecules was obvious in STM and  $\text{Cu}_2\text{O}$  NSs remained intact. While CO molecules could adsorb on bulk  $\text{Cu}_2\text{O}$  surfaces at cryogenic temperatures<sup>36</sup>, the interaction between CO and supported  $\text{Cu}_2\text{O}$  NSs appeared to be much weakened by OMI. Owing to the weak interaction between CO and  $\text{Cu}_2\text{O}/\text{Au}(111)$ , CO exposure under vacuum conditions did not cause any change on the  $\text{Cu}_2\text{O}/\text{Au}(111)$  surface at 300 K. However, as the partial pressure of CO was raised to 0.5 mbar, enhanced CO adsorption could cause the continuous reduction of  $\text{Cu}_2\text{O}$  NSs to form the Cu–Au surface alloy (Fig. 3c–h). In situ NAP-STM images showed further that the reduction started from the edges of  $\text{Cu}_2\text{O}$  NSs on  $\text{Au}(111)$  (Supplementary Fig. 9). When the  $\text{Au}(111)$  surface was fully covered by  $\text{Cu}_2\text{O}$ , the onset pressure for the reduction of the  $\text{Cu}_2\text{O}$  layer needs be further raised to  $\sim 6$  mbar CO in our NAP-STM study. Thus, both the activity and the stability of supported  $\text{Cu}_2\text{O}$  NSs are influenced by OMI.

While CO oxidation occurred readily at the  $\text{Cu}_2\text{O}/\text{Pt}(111)$  and the  $\text{Cu}_2\text{O}/\text{Au}(111)$  interface under UHV and NAP conditions, respectively, no appreciable activities of CO oxidation were observed on the  $\text{Cu}_2\text{O}/\text{Ag}(111)$  surface in 10 mbar CO at 300 K (Fig. 4 and Supplementary Fig. 10), despite  $\text{Cu}_2\text{O}$  exposes the same zig-zag edge structure on  $\text{Ag}(111)$  as those on  $\text{Pt}(111)$  and  $\text{Au}(111)$  and the adsorption energy of CO on  $\text{Ag}(111)$  is similar to that on  $\text{Au}(111)$ <sup>37</sup>. Indeed, even when CO pressure was raised to  $\sim 48$  mbar, the zig-zag edges of  $\text{Cu}_2\text{O}$  on  $\text{Ag}(111)$  could not react with CO at 300 K, whereas one could start to observe the reduction of  $\text{Cu}_2\text{O}$  from low-coordination sites at the domain

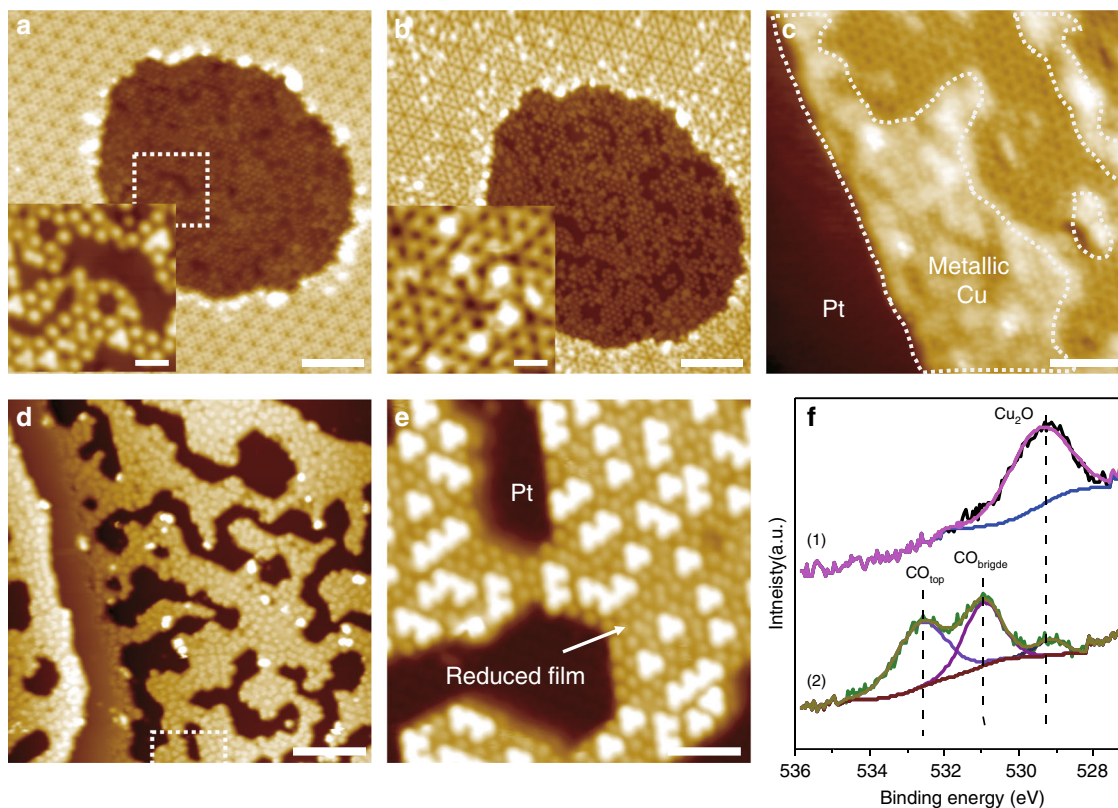


**Fig. 2 The adsorption and reaction of CO on Cu<sub>2</sub>O/Pt(111).** **a, b** In situ STM images of the Cu<sub>2</sub>O/Pt(111) surface during the exposure to CO at 78 K. The squared region in **a** is magnified in inset, showing CO adsorption on a Pt(111) surface covered by (2 × 2)-O. Inset in **b** displays the adsorption sites of CO on Cu<sub>2</sub>O, which are centered at the holes of the Cu<sub>2</sub>O rings. **c** STM image of the partially reduced Cu<sub>2</sub>O/Pt(111) surface after the surface in **b** was annealed to 300 K. The reduction by CO started from both the step edge and the surface of Cu<sub>2</sub>O. The dotted curves indicate the regions of metallic Cu. **d, e** STM images of a Cu<sub>2</sub>O/Pt(111) surface after the exposure to 1 × 10<sup>-7</sup> mbar CO for 5 min at 300 K. High-resolution STM image (**e**) from the marked area in **d** shows the reduction of Cu<sub>2</sub>O by CO led to the formation of triangular Cu<sub>3</sub>O<sub>x</sub> clusters, sitting on a metallic layer. **f** XPS O 1s spectra of the Cu<sub>2</sub>O/Pt(111) surface before (1) and after (2) the exposure to 1.2 × 10<sup>-7</sup> mbar CO for 5 min at 300 K. Lattice O of Cu<sub>2</sub>O with binding energy at 529.4 eV has been mostly consumed after CO exposure, accompanying the adsorption of CO on top sites (CO<sub>top</sub>) and bridge sites (CO<sub>bridge</sub>) of the exposed Pt surface. Scanning parameters: **b** V<sub>s</sub> = -0.3 V, I = 0.2 nA; inset: V<sub>s</sub> = -0.3 V, I = 0.5 nA; **c** V<sub>s</sub> = -0.15 V, I = 1.2 nA; **e** V<sub>s</sub> = -0.15 V, I = 0.5 nA. Scale bars: **a, b** 5 nm, inset 1 nm; **c** 3 nm; **d** 10 nm; **e** 2 nm.

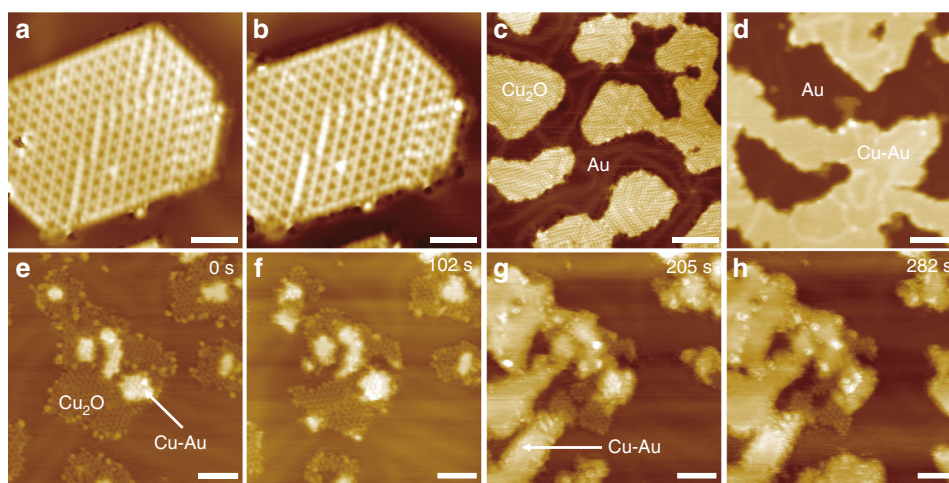


**Fig. 3 The adsorption and reaction of CO on Cu<sub>2</sub>O/Au(111).** **a, b** In situ STM images before (**a**) and after (**b**) the exposure of CO on Cu<sub>2</sub>O/Au(111) at 78 K. No adsorption was obvious after the exposure of 18 L CO. **c, d** Ex-situ and **e-h** in situ NAP-STM images on the reduction of Cu<sub>2</sub>O on Au(111) in 1 mbar (**d**) or 0.5 mbar (**e-h**) CO at 300 K. The reduction of Cu<sub>2</sub>O NSs led to the formation of a Cu-Au surface alloy. The reaction times were marked at the top right of images. Scanning parameters: **a** V<sub>s</sub> = -2.0 V, I = 0.06 nA; **b** V<sub>s</sub> = -1.7 V, I = 0.03 nA; **c** V<sub>s</sub> = 1.1 V, I = 0.09 nA; **e** V<sub>s</sub> = 1.2 V, I = 0.02 nA; **f** V<sub>s</sub> = 1.2 V, I = 0.05 nA. Scale bars: **a, b** 2 nm; **c, d** 10 nm; **e-h** 5 nm.

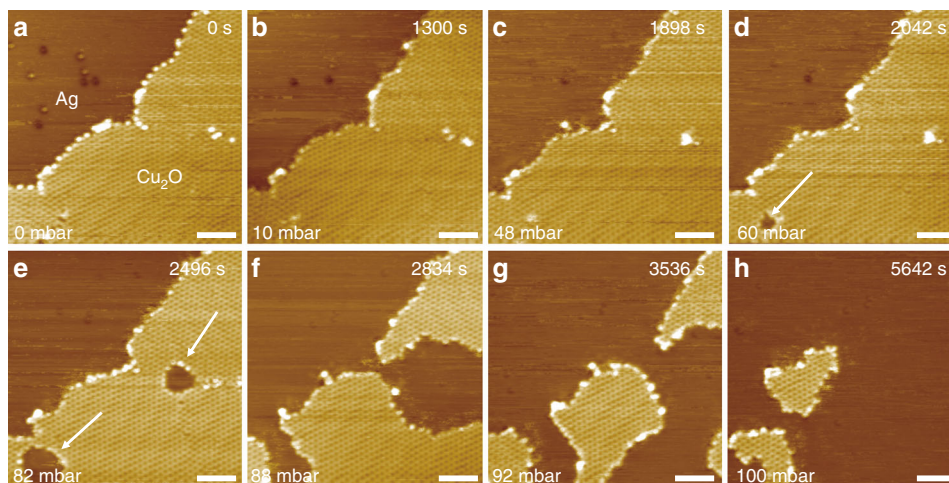


**Fig. 4** Reaction of CO on Cu<sub>2</sub>O/Ag(111). **a–h** In situ NAP-STM images on the reduction of the Cu<sub>2</sub>O/Ag(111) surface under elevated CO pressures from 0 to 100 mbar at 300 K. Reduction of the Cu<sub>2</sub>O layer was observed in >48 mbar CO, starting from domain boundaries indicated by white arrows in **d, e**. The pressures of CO were labeled at the bottom left of STM images, and reaction times were labeled at the top right of images. Scanning parameters: **a–h**  $V_s = 0.9$  V,  $I = 0.1$  nA. Scale bars: 5 nm for all images.

boundaries of Cu<sub>2</sub>O. The inactivity of the zig-zag edges of Cu<sub>2</sub>O on Ag(111) is in drastic contrast to the active zig-zag edges of Cu<sub>2</sub>O on Au(111) and Pt(111), where the onset reaction pressures are in the ranges of  $10^{-1}$  and  $10^{-8}$  mbar CO, respectively. Thus, the reactivity trend of the Cu<sub>2</sub>O/M interface follows the order of: Cu<sub>2</sub>O/Pt(111) > Cu<sub>2</sub>O/Au(111) > Cu<sub>2</sub>O/Ag(111). Note that, the rate equation could be affected by both the surface coverage of CO and the activation energy. Since the adsorption energies of CO are approximately similar ( $-0.29$  eV)<sup>37</sup> on Au(111) and Ag(111), the reactivity comparison between Cu<sub>2</sub>O/Au(111) and Cu<sub>2</sub>O/Ag(111) could indeed rule out influence of surface CO coverage and corroborated further the critical role of OMI in tuning the activation barrier and thus reactivity of the oxide–metal interface.

The regeneration of Cu<sub>2</sub>O NSs is important to complete the catalytic cycle of CO oxidation. We found that the re-oxidation of the Pt–Cu surface alloy on CO-covered Pt(111) requires only an O<sub>2</sub> atmosphere at  $5 \times 10^{-8}$  mbar (at >400 K) to form well-ordered Cu<sub>2</sub>O NSs (Supplementary Fig. 11a), whereas the Au–Cu surface alloy remained metallic in  $5 \times 10^{-7}$  mbar O<sub>2</sub> at 450 K (Supplementary Fig. 11b). But, Cu<sub>2</sub>O NSs were found to grow from the steps of the Au–Cu surface alloy on Au(111) in  $\sim 1$  mbar O<sub>2</sub> at 300 K (Supplementary Fig. 11c). Similarly, Cu on Ag(111) could be oxidized into Cu<sub>2</sub>O in 0.17 mbar O<sub>2</sub>, accompanying the oxidation of Ag(111) (Supplementary Fig. 11d). In this case, CO oxidation on the Cu<sub>2</sub>O/Ag(111) surface could be a convoluted process since Ag(111) could also be oxidized by O<sub>2</sub> under NAP conditions<sup>38</sup>. Yet, the redox cycle of supported Cu<sub>2</sub>O NSs should exhibit a lower barrier on Pt(111) than on Au(111) and Ag(111). Although group IB precious metals do not suffer from the CO-poisoning problem, their weak interaction with CO and O<sub>2</sub><sup>39,40</sup> are not favorable for maintaining an active Cu<sub>2</sub>O–metal interface, which appears crucial for a sustained catalytic activity in low temperature CO oxidation. Owing to the strong chemisorption of CO on Pt group metals, the presence of excess O<sub>2</sub> or the increase of reaction temperature should be beneficial to sustain the active Cu<sub>2</sub>O–metal interface for CO oxidation.

**Catalytic performance for CO oxidation.** To examine the role of OMI in tuning the catalytic activity of supported Cu<sub>2</sub>O NSs, we prepared further PtCu, AuCu and AgCu alloy nanoparticle catalysts supported on carbon black (CB) and measured their

catalytic performances in CO oxidation as a function of temperature and under O<sub>2</sub>-rich conditions (oxide supports were avoided to reduce the complexity of interfacial interaction). Previous studies<sup>24,26,41</sup> have shown that Cu atoms in bimetallic nanoparticles would segregate to the surface to form oxide layer under oxidative conditions, which is typical for cheap metals in bimetallic alloys<sup>6,12,42</sup>. The chemical states of these catalysts were confirmed further in the post-reaction analysis using quasi-in situ XPS (Supplementary Fig. 12), where the XPS chamber is attached with a high-pressure reactor for catalytic studies. XPS measurements showed that, after reaction, Cu in the PtCu/CB and AuCu/CB catalysts remained as Cu<sub>2</sub>O from the Cu 2p and Cu Auger spectra<sup>43</sup>, whereas Cu in the AgCu/CB catalyst was oxidized into CuO. The size and structure of alloy nanoparticle catalysts were examined by transmission electron microscopy (TEM, Supplementary Fig. 13). The particle morphology appeared similar before and after reaction, except that the ripening of particles could be observed.

Figure 5 compared the light-off curves of the series of catalysts in CO oxidation, where the catalytic performances of Cu<sub>2</sub>O powders and Pt, Au, and Ag nanoparticles supported on CB (denoted as Pt/CB, Au/CB, and Ag/CB, respectively) were also measured for comparison. Consistent with the above model studies, the PtCu/CB catalyst exhibited appreciable activity for CO oxidation right above 300 K, whereas Pt/CB showed neglectable CO conversion at below the CO desorption temperature ( $\sim 400$  K)<sup>44</sup>. The activity of the AuCu/CB catalyst is also superior to those of Cu<sub>2</sub>O and Au/CB catalysts, and showed activity at above 300 K, although the increase of CO conversion is slower than that of PtCu/CB catalyst. The activities of AgCu/CB and Ag/CB catalysts (Supplementary Fig. 14) were not plotted with above catalysts for comparison, since the operation of these catalysts did not suffer CO poisoning and involved surface oxidation of Ag<sup>38,45</sup> (as evidenced in Supplementary Fig. 11). As Ag alone showed good activity for CO oxidation under O<sub>2</sub>-rich conditions, the formation of CuO<sub>x</sub>/Ag interface reduced the activity of Ag for CO oxidation, which could be attributed to the covering of active Ag sites and consistent with the above STM study. Weak OMI in Cu<sub>2</sub>O/Ag is insufficient to maintain the active Cu<sup>+</sup> state, leading to the formation of CuO (Supplementary Fig. 12) and the decrease of reactivity. By comparison, the formation of Cu<sub>2</sub>O/M interfaces indeed annihilate the CO poisoning problem suffered by Pt group metals and the reactivity

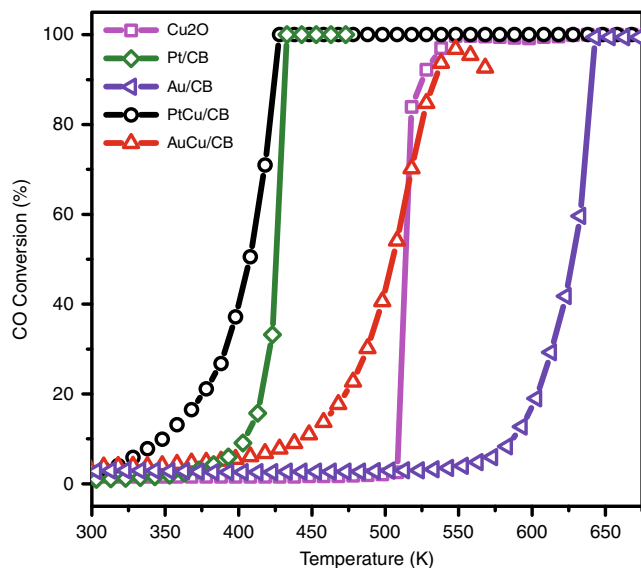


**Fig. 5 Catalytic performance of the PtCu/CB, Pt/CB, AuCu/CB, Au/CB and Cu<sub>2</sub>O catalysts.** The light-off curves for CO oxidation were obtained under the condition of 1% CO, 20% O<sub>2</sub>, and 79% He. Space velocity was 60,000 mL g<sup>-1</sup> h<sup>-1</sup>.

from powder catalytic measurements agree with the model studies in the order of: Cu<sub>2</sub>O/Pt > Cu<sub>2</sub>O/Au > Cu<sub>2</sub>O/Ag, which again confirmed the activities of Cu<sub>2</sub>O NSs are tuned by OMI.

**Analysis on the oxide-metal interaction.** Spin-polarized DFT calculations were further conducted to understand the nature of OMI in tuning the activities of supported Cu<sub>2</sub>O NSs. Based on the atomic structures determined from ES-STM, structural models of M(111)-supported (M = Pt, Au, Ag) and freestanding Cu<sub>8</sub>O<sub>6</sub> nanoribbons were constructed, denoted as Cu<sub>2</sub>O/M and Cu<sub>2</sub>O-fs. After structural optimization, these models showed the honeycomb lattice of an O-Cu-O tri-layer with O-terminated zig-zag edges (Fig. 6a), consistent with STM results. To understand the above model catalytic studies, we looked into the reaction between CO and O of supported Cu<sub>8</sub>O<sub>6</sub> nanoribbons (Fig. 6b-d). STM study (Supplementary Fig. 6) showed that the reduction of Cu<sub>3</sub>O<sub>2</sub> occurred mainly at edge O sites. We thus considered mainly the reaction between CO and edge O atoms in supported Cu<sub>8</sub>O<sub>6</sub> nanoribbons. The energy of CO in gas phase was corrected as the Gibbs free energy of CO under UHV conditions (1 × 10<sup>-7</sup> mbar).

For the Cu<sub>2</sub>O/Au and Cu<sub>2</sub>O/Ag systems, the Gibbs free energy barrier for transition state 1 (TS1, Fig. 6b, d) corresponds to the energy difference between TS1 and CO in gas phase since CO adsorption is not preferred under UHV conditions and the free energy barrier increases linearly to the decrease of the logarithm of CO pressure (Supplementary Figs. 15, 16). The reaction diagrams (Fig. 6b, d) suggested that the rate determining step is the formation of CO<sub>2</sub>, where the barrier on Cu<sub>2</sub>O/Pt (0.42 eV) is lower than those on Cu<sub>2</sub>O/Au (0.60 eV) and Cu<sub>2</sub>O/Ag (0.86 eV). The high activity of the Cu<sub>2</sub>O/Pt interface could be interpreted via a dual-site mechanism<sup>12,46</sup> that Pt(111) provides proper CO adsorption while the interface between Pt and edge Cu sites enables O<sub>2</sub> dissociation (Supplementary Fig. 17) via a low dissociation barrier (0.39 eV), which is also thermodynamically favored. In comparison, O<sub>2</sub> dissociation at Cu<sub>2</sub>O/Au and Cu<sub>2</sub>O/Ag interfaces are thermodynamically less-favorable, although the process was still enhanced by OMI, when compared with those on Au(111) and Ag(111)<sup>37</sup>.

We then look further into geometric and electronic factors that could be utilized to quantify the role of OMI in dictating the activity of Cu<sub>2</sub>O/M systems. Typically, the adhesion energy ( $E_{adh}$ ) has been used to quantify OMI, which for Cu<sub>8</sub>O<sub>6</sub> nanoribbon on M(111), gives the order of Cu<sub>2</sub>O/Pt (-0.76 eV) > Cu<sub>2</sub>O/Ag (-0.71 eV) > Cu<sub>2</sub>O/Au (-0.58 eV). This is obviously inconsistent with the reactivity order observed in the above experimental studies and indicates that the dual interaction of Cu/O atoms with M(111) could be not directly relevant to the key reaction steps, i.e., the formation of CO<sub>2</sub> and the subsequent formation of O vacancy in Cu<sub>2</sub>O. In this case, oxygen vacancy formation energy ( $E_{Ovf}$ ) should be of direct relevance and indeed we found the order of  $E_{Ovf}$  for supported Cu<sub>2</sub>O NSs tracks the same order as their catalytic activities (Cu<sub>2</sub>O/Pt > Cu<sub>2</sub>O/Au > Cu<sub>2</sub>O/Ag, Fig. 6c). Further, compared with  $E_{Ovf}$  on the edge of Cu<sub>2</sub>O-fs (-0.39 eV),  $E_{Ovf}$  for supported Cu<sub>2</sub>O NSs are much more negative, in the range of -1.33 ~ -2.35 eV, suggesting the formation of oxygen vacancy is much facilitated at the edges of Cu<sub>2</sub>O/M. Thus, OMI plays a key role in weakening the Cu-O bond and facilitating the removal of O atoms by CO. The stronger OMI, the easier the removal of O and the formation of CO<sub>2</sub>.

As we looked into the process of O removal, the interaction between M(111) and Cu<sup>+</sup> (the formation of Cu-M bond after the removal of O, Supplementary Fig. 18) is found as a key descriptor for the formation of O vacancies (Fig. 7). We calculated the projected density of states on *d* orbitals of Cu atoms on the edge of Cu<sub>2</sub>O-fs and M atoms from the surface layer of M(111) clean surface (M = Pt, Au, Ag) and their corresponding *d* band centers ( $\epsilon_d$ , Fig. 7a). According to the *d*-band theory<sup>47</sup>, when the  $\epsilon_d$  of M is closer to the Fermi level, the stronger interaction of metal surface with Cu<sup>+</sup> could be expected since the *d* band for Cu<sup>+</sup> is relatively localized (molecule like, Fig. 7a). Therefore, the bonding strength between M(111) and Cu<sup>+</sup> follows the order of Cu<sub>2</sub>O/Pt > Cu<sub>2</sub>O/Au > Cu<sub>2</sub>O/Ag, consistent with the rank order of  $E_{Ovf}$  and the catalytic activity. Quantitatively, we use the distance between  $\epsilon_d$  of Cu<sub>2</sub>O and  $\epsilon_d$  of M(111) to describe the electronic interaction between Cu<sup>+</sup> and M. Assuming  $\epsilon_d$  of Cu<sub>2</sub>O at a fixed value, the differences in electronic interaction among Cu<sub>2</sub>O/M could be represented by the differences in  $\epsilon_d$  of M. As we plotted  $E_{Ovf}$  as a function of  $\epsilon_d$  for M(111) in Fig. 7b, an excellent scaling relationship could be observed. Note that, geometric factors, such as surface rumpling ( $\Delta h$ ), has also been used to describe the formation energy of O vacancies on oxide surfaces.<sup>48</sup> But, our study found that surface rumpling cannot be used to describe the Cu<sub>2</sub>O-M interface, because the order of  $\Delta h$  for Cu<sub>8</sub>O<sub>6</sub> nanoribbons on metal substrates is: Cu<sub>2</sub>O/Pt (0.46 Å) > Cu<sub>2</sub>O/Ag (0.40 Å) > Cu<sub>2</sub>O/Au (0.34 Å), inconsistent with their reactivity order. Therefore, OMI should be described by the electronic interaction between Cu<sub>2</sub>O and metal substrates, where  $\epsilon_d$  could be used as a simple descriptor. Pt group metals are favored over group IB metals for interfacial catalysis of CO oxidation, due to the much stronger OMI that lowers/stabilizes greatly the reaction energy surfaces. We identify the interaction between M(111) and Cu<sup>+</sup> as a key descriptor to quantify the role of OMI in dictating the reactivity of Cu<sub>2</sub>O/M in CO oxidation. The stronger interaction of M(111) with Cu<sup>+</sup> enables the higher activity of Cu<sub>2</sub>O/M for catalytic oxidation.

To understand the catalytic properties of the Cu<sub>2</sub>O-metal interface, well-defined Cu<sub>2</sub>O NSs were synthesized on a series of M(111) (M = Pt, Au, Ag) single crystals and studied at the atomic scale using LT-STM, NAP-STM, XPS, and DFT calculations. The surface and step structures of supported Cu<sub>2</sub>O NSs were identified unambiguously in ES-STM images, which show the same Cu<sub>3</sub>O<sub>2</sub> honeycomb lattice for the above Cu<sub>2</sub>O NSs, with similar unit cell length and a dominant O-terminated zig-zag edge. Despite their structural similarity, supported Cu<sub>2</sub>O NSs

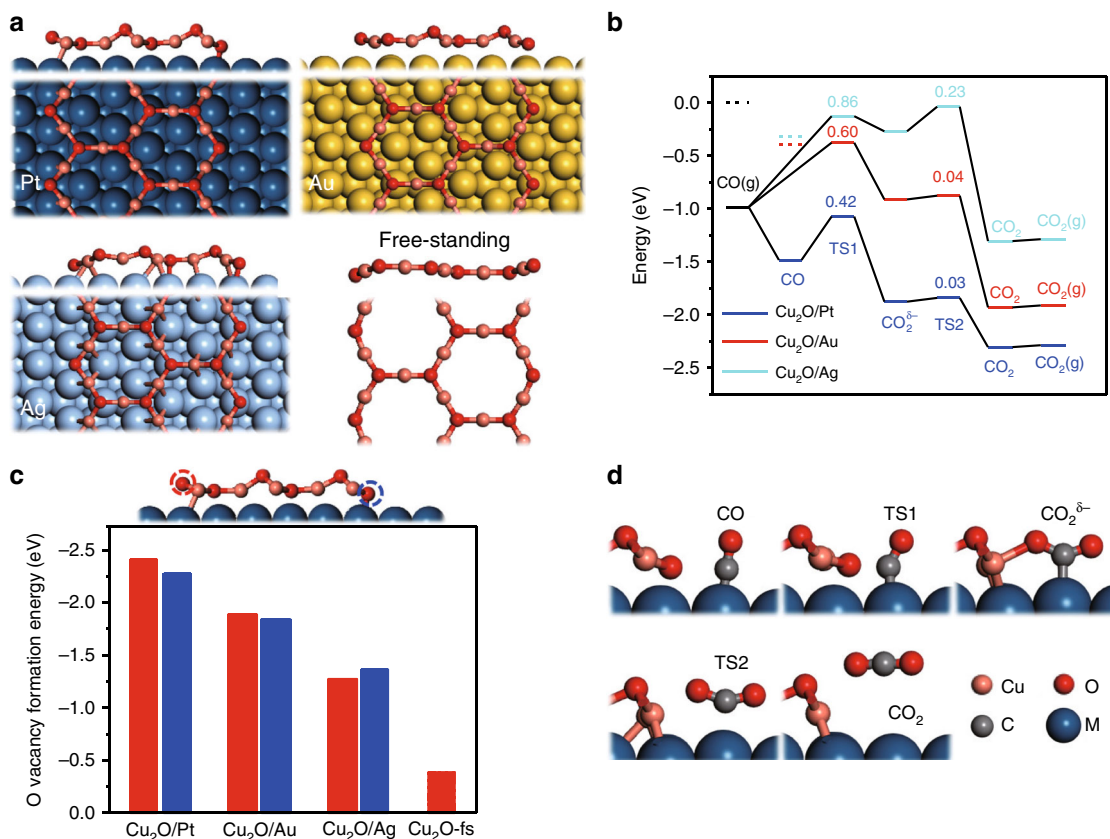


**Fig. 6** DFT calculations about CO oxidation reaction on supported Cu<sub>2</sub>O NSs. **a** DFT-optimized structures of Pt(111), Au(111), Ag(111) supported and freestanding Cu<sub>2</sub>O nanoribbons (denoted as Cu<sub>2</sub>O/M (M=Pt, Au, Ag) and Cu<sub>2</sub>O-fs). **b** Potential energy diagram for the reaction between CO and O on the stabilized edge of M(111) supported Cu<sub>2</sub>O NSs. The value of barrier is labeled above the corresponding transition state (unit: eV). The energy of CO(g) is represented as the Gibbs free energy of CO under UHV conditions ( $1 \times 10^{-7}$  mbar) while the black dashed bar at 0 eV marks the DFT-calculated energy of CO without corrections. The red and cyan dashed bars mark the adsorption energy of CO on the top site of Au(111) and Ag(111) surface near the edge of Cu<sub>2</sub>O NSs. **c** The formation energy of O vacancy for two kinds of O atoms, marked by red and blue dashed circles, at the edges of Cu<sub>2</sub>O/M and Cu<sub>2</sub>O-fs. **d** The optimized structures for reaction intermediates and transition states (adsorbed CO, transition state 1 (TS1), CO<sub>2</sub> adsorbed with bending configuration, transition state 2 (TS2) and CO<sub>2</sub> adsorbed with straight configuration) in **b**.

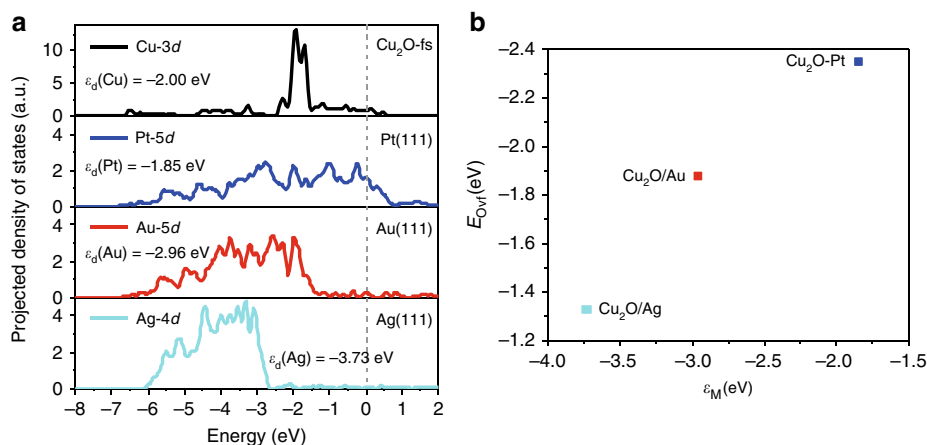


**Fig. 7** Electronic interaction between Cu<sub>2</sub>O-fs and M(111). **a** Density of states projected on *d* orbitals of Cu atoms on the edge of Cu<sub>2</sub>O-fs and M atoms from the surface layer of M(111) (M = Pt, Au, Ag) and their corresponding *d* band centers. The grey dashed line marks the Fermi level. **b**  $E_{Ovf}$  for O atoms at the edge of Cu<sub>2</sub>O/M as a function of *d* band center of M(111).

exhibit a substrate-dependent thermal stability. Cu<sub>2</sub>O NSs on Pt (111) showed a surprisingly low stability, with an onset decomposition temperature even lower than the desorption temperature of oxygen atoms on Pt(111). In contrast, Cu<sub>2</sub>O

NSs on Ag(111) and Au(111) remained stable in UHV even after the annealing at up to 700 K.

As we compared the reactivities of Cu<sub>2</sub>O NSs on M(111) for CO oxidation, we found all surfaces could react with CO at room

temperature. But, the reduction of  $\text{Cu}_2\text{O}$  on Pt(111) needs only a CO pressure at  $5 \times 10^{-8}$  mbar, whereas the reduction of  $\text{Cu}_2\text{O}$  on Au(111) requires a CO pressure at 0.5 mbar, and even much higher on Ag(111). Vice versa, the regeneration of  $\text{Cu}_2\text{O}$  NSs needs only  $5 \times 10^{-8}$  mbar  $\text{O}_2$  on Pt(111), while the regeneration of  $\text{Cu}_2\text{O}$  NSs requires NAP conditions on Au(111) ( $\sim 1$  mbar  $\text{O}_2$ ) and Ag(111) ( $\sim 0.2$  mbar  $\text{O}_2$ ). Further catalytic tests on powder samples corroborated that the interface with  $\text{Cu}_2\text{O}$  NSs could annihilate the CO-poisoning problem and enable low temperature CO oxidation on Pt group metals. The reactivity of supported  $\text{Cu}_2\text{O}$  NSs is found determined and much enhanced by OMI, when compared with  $\text{Cu}_2\text{O}$ -fs. The analysis of reaction mechanism and OMI showed that OMI facilitates CO oxidation by enhancing the activity of interfacial oxygen atoms and stabilizing oxygen vacancies in  $\text{Cu}_2\text{O}$  NSs. The stronger the OMI, the lower the barrier for CO oxidation catalyzed by supported  $\text{Cu}_2\text{O}$  NSs. The role of OMI in dictating the activity and stability of supported  $\text{Cu}_2\text{O}$  NSs could be described by the formation energy of interfacial oxygen vacancy. Further,  $d$  band center could serve as a simple descriptor for OMI to correlate the electronic interaction between  $\text{Cu}^+$  and metal substrates with the formation energy of oxygen vacancy and the reactivity of  $\text{Cu}_2\text{O}/\text{M}$  interfaces for CO oxidation. Thus, our study provides insight for OMI and a strategy for the design of oxide NS catalysts for oxidation reactions.

## Methods

**Model catalyst synthesis and characterization.** The experiments were carried out in two UHV systems. The first system consists of a CreaTec LT-STM with base pressure at  $< 4 \times 10^{-11}$  mbar and a preparation chamber equipped with XPS, and cleaning facilities. LT-STM measurements were conducted at 78 K, using an electrochemically etched W tip. The second system consists of a SPECS NAP-STM with base pressure  $< 2 \times 10^{-10}$  mbar and a preparation chamber equipped with cleaning facilities. NAP-STM measurements were conducted at 300 K using a Pt-Ir tip. Pt(111), Au(111), and Ag(111) single crystals (Mateck) were cleaned by cycles of  $\text{Ar}^+$  sputtering at 1.2 kV and annealing to 800 K for Au(111) and Ag(111) or 1000 K for Pt(111) until no impurities were obvious on the surface from STM.

Well-ordered  $\text{Cu}_2\text{O}$  NSs of ML thickness could be synthesized on metal single crystals by evaporating Cu in  $1 \times 10^{-7}$  mbar  $\text{O}_2$  at cryogenic temperatures, which were followed by the annealing in  $\text{O}_2$  at  $\sim 500$  K. To obtain well-ordered structure,  $\text{Cu}_2\text{O}/\text{Au}(111)$  and  $\text{Cu}_2\text{O}/\text{Ag}(111)$  could be annealed in UHV condition above 500 K. On Au(111),  $\text{Cu}_2\text{O}$  NSs could be prepared by depositing Cu in  $\sim 3 \times 10^{-7}$  mbar  $\text{NO}_2$  at 300 K, which were followed by the annealing in  $\text{NO}_2$  at 400 K.  $\text{Cu}_2\text{O}/\text{Ag}(111)$  could also be prepared by oxidation of  $\text{Cu}/\text{Ag}(111)$  by near ambient pressure of  $\text{O}_2$  at 300 K. Then to remove the surface Ag-O species,  $\text{Cu}_2\text{O}/\text{Ag}(111)$  was annealed at  $\sim 450$  K. For all experiments,  $\text{O}_2$  and CO were purified by liquid nitrogen for over 1 h to remove impurities before being introduced into the chambers. Different modes of ES-STM images were acquired using W tip and controlling the indentation of W tip into the  $\text{Cu}_2\text{O}$  surface to obtain a  $\text{CuO}_x$ -terminated tip<sup>29,49</sup>. All STM images were processed with SPIP software (Image Metrology). XPS characterization of  $\text{Cu}_2\text{O}/\text{Pt}(111)$  was conducted with Mg-K $\alpha$  energy source ( $h\nu = 1253.6$  eV). The binding energies were calibrated with that of Pt 4f<sub>7/2</sub> signal located at 71.0 eV.

Powder catalysts preparation and catalytic tests. PtCu/CB catalyst was prepared by co-impregnation method. First, 100 mg CB (Vulcan XC-72) were dispersed into 5 mL  $\text{H}_2\text{O}$  by ultrasonic treatment for 0.5 h. Next the aqueous solutions of  $\text{H}_2\text{PtCl}_6$  and  $\text{Cu}(\text{NO}_3)_2$  were successively added. The nominal loading of Pt was 4 wt%, and the molar ratio of Cu to Pt was 1:4. Then, excess water was evaporated at room temperature under continuous agitation (500 rpm). Finally, the solid was dried at 333 K in an oven for 12 h to obtain the catalyst for use. The preparation procedures for AuCu/CB and AgCu/CB catalysts were exactly the same as that for PtCu/CB by only replacing the precursor into  $\text{HAuCl}_4$  or  $\text{AgNO}_3$  respectively. Pt/CB, Au/CB, and Ag/CB were prepared in similar manner but without addition of  $\text{Cu}(\text{NO}_3)_2$ . The  $\text{Cu}_2\text{O}$  powder (99% purity) was bought from Energy Chemical.

CO oxidation was carried out in a fixed-bed reactor. The reactant gas consisted of 1% CO, 20%  $\text{O}_2$ , and 79% He (Messer). The reactant gas was flowed at  $20 \text{ mL min}^{-1}$  through 20 mg catalyst to achieve a space velocity of  $60,000 \text{ mL g}^{-1} \text{ h}^{-1}$ . The tail gas was analyzed online by gas chromatography equipped with methane converter in front of flame ionization detector. Before reactions, all catalysts were reduced in high-purity  $\text{H}_2$  flow at 473 K for 2 h. After cooling down in high-purity Ar flow, samples were kept in reactant gas for 1 h at 298 K, then temperature-dependent CO oxidation was performed from room temperature to 573–673 K at a rate of  $1 \text{ K min}^{-1}$ .

XPS analysis of powder catalysts were performed in ThermoFischer ESCALAB 250Xi photoelectron spectrometer using monochromated X-ray irradiation Al-K $\alpha$  ( $h\nu = 1486.7$  eV) and  $180^\circ$  double focusing hemispherical analyzer with a six-channel detector. The binding energies of the photoemission spectra were calibrated to C 1s peak at 284.4 eV. The XPS chamber is attached with a high-pressure reactor for catalytic studies. Samples were reduced in pure hydrogen (1 bar) to 473 K for 1 h and then cooled to 300 K in  $\text{H}_2$ . CO oxidation reaction was then performed in the mixture gas (1 bar, 1% CO and 20%  $\text{O}_2$  with He balance) to 400 K for PtCu/CB or 500 K for AuCu/CB and AgCu/CB. After reaction, the sample was cooled to room temperature in reactant gas. XPS measurements were performed after evacuating the reactor cell and transferring the samples in UHV into the analyzer chamber without air exposure.

**Computational method.** Theoretical calculations were carried out based on density functional theory (DFT) framework by using Vienna ab initio simulation packages (VASP)<sup>50</sup> with the projector augmented wave (PAW)<sup>51</sup> scheme and the plane-wave basis set with the cutoff energy of 400 eV were adopted<sup>52</sup>. The generalized gradient approximation (GGA) functional developed by Perdew–Burke–Ernzerhof (PBE)<sup>53</sup> for the exchange-correlation term was used. The method of Methfessel-Paxton was employed to define the partial occupancies of metal-supported or freestanding  $\text{Cu}_8\text{O}_6$  (each supercell includes 8 Cu and 6 O) ribbon. Climbing image nudged elastic band (NEB) method<sup>54,55</sup> was used for searching of transition states. All the models were well converged until the forces decreased to less than  $0.05 \text{ eV \AA}^{-1}$ . Models of  $\text{Cu}_8\text{O}_6$  nanoribbons on Pt(111), Au(111), and Ag(111) were adopted. For each model, a 4-layer  $2 \times 4\sqrt{3}$  supercell of M(111) ( $M = \text{Pt, Au, Ag}$ ) surface was used as substrate. Gamma-centered K-mesh of  $4 \times 4 \times 1$  was employed for structure optimization or transition-state searching. 4-layer  $4 \times 4$  M(111) ( $M = \text{Pt, Au, Ag}$ ) surface with Gamma-centered K-mesh of  $4 \times 4 \times 1$  were adopted as reference of pure metal for CO adsorption calculations. For all models, the vacuum was set to be about 12 Å. During structure optimization, the bottom layer of substrate was constrained while the rest parts were fully relaxed. Freestanding  $\text{Cu}_8\text{O}_6$  nanoribbon was fully relaxed at the fixed lattice in bulk value ( $6.105 \text{ \AA}$ ) with the Gamma-centered K-mesh  $4 \times 4 \times 1$ .

The  $d$  band center ( $\epsilon_d$ ) was calculated through the formula<sup>56</sup> below:

$$\epsilon_d = \frac{\int_{-\infty}^{\infty} n_d(\epsilon)\epsilon d\epsilon}{\int_{-\infty}^{\infty} n_d(\epsilon) d\epsilon}, \quad (1)$$

where  $\epsilon$  is energy and  $n_d(\epsilon)$  is the density of states of electrons. Integral interval is from negative infinity to positive infinity.

Surface rumpling was defined as  $\Delta h$ , which is calculated through the formula:

$$\Delta h = \frac{\sum_{i=1}^n |h_{\text{O}_i} - \overline{h_{\text{Cu}}}|}{n}, \quad (2)$$

where  $h_{\text{O}_i}$  is the height of the  $i$ th O,  $\overline{h_{\text{Cu}}}$  is the average height of Cu,  $n$  is the number of O in  $\text{Cu}_8\text{O}_6$  nanoribbon.

Adhesion energy  $E_{\text{adh}}$  was calculated through the formula:

$$E_{\text{adh}} = E_{\text{tot}} - E_{\text{oxi}} - E_{\text{M}}, \quad (3)$$

where  $E_{\text{tot}}$  is DFT-calculated total energy for M(111) supported  $\text{Cu}_8\text{O}_6$  nanoribbon;  $E_{\text{oxi}}$  and  $E_{\text{M}}$  are energy for freestanding  $\text{Cu}_8\text{O}_6$  nanoribbon and M(111), respectively.

Oxygen vacancy formation energy ( $E_{\text{Ovf}}$ ) is the energy needed to remove one oxygen from  $\text{Cu}_8\text{O}_6$  nanoribbons, referencing to CO and  $\text{CO}_2$  in gas phase, which is calculated through the formula below:

$$E_{\text{Ovf}} = E_{\text{Ovac}} + E_{\text{CO}_2} - E_{\text{CO}} - E_{\text{per}}, \quad (4)$$

where  $E_{\text{Ovac}}$  and  $E_{\text{per}}$  are DFT-calculated total energy for structures with one oxygen vacancy and without that, respectively;  $E_{\text{CO}_2}$  and  $E_{\text{CO}}$  are energy for  $\text{CO}_2$  and CO in gas phase.

The Gibbs free energy of CO ( $G_{\text{CO}}$ ) in gas phase is calculated through the formula below:

$$G_{\text{CO}} = E_{\text{elec}} + \text{ZPE} + \int C_p dT - TS + kT \ln p_{\text{CO}}/p_0, \quad (5)$$

where  $E_{\text{elec}}$  is the electronic energy calculated via VASP; ZPE is the zero-point energy,  $\int C_p dT$  is the variety of isobaric heat capacity as the temperature changes,  $S$  is entropy and  $T$  is 298 K.  $p_{\text{CO}}$  and  $p_0$  is the pressure of CO and the standard atmosphere (1000 mbar) respectively;  $k$  is the Boltzmann constant. The results of ZPE,  $\int C_p dT$ ,  $S$  is given by the ASE (atomic simulation environment) code<sup>57</sup>.

## Data availability

All data supporting this work are available from the corresponding author upon reasonable request.

Received: 20 July 2019; Accepted: 2 April 2020;

Published online: 08 May 2020



## References

1. Yu, W., Porosoff, M. D. & Chen, J. G. Review of Pt-based bimetallic catalysis: from model surfaces to supported catalysts. *Chem. Rev.* **112**, 5780–5817 (2012).
2. Thayer, A. M. Catalyst suppliers face changing industry. *Chem. Eng. News* **70**, 27–49 (1992).
3. Guo, Z. et al. Recent advances in heterogeneous selective oxidation catalysis for sustainable chemistry. *Chem. Soc. Rev.* **43**, 3480–3524 (2014).
4. Armor, J. N. Environmental catalysis. *Appl. Catal. B* **1**, 221–256 (1992).
5. Grimaud, A., Hong, W. T., Shao-Horn, Y. & Arason, J. M. Anionic redox processes for electrochemical devices. *Nat. Mater.* **15**, 121–126 (2016).
6. Wu, C. H. et al. Bimetallic synergy in cobalt–palladium nanocatalysts for CO oxidation. *Nat. Catal.* **2**, 78–85 (2019).
7. Zavabeti, A. et al. A liquid metal reaction environment for the room-temperature synthesis of atomically thin metal oxides. *Science* **358**, 332–335 (2017).
8. Tauster, S. J., Fung, S. C. & Garten, R. L. Strong metal-support interactions. Group 8 noble metals supported on titanium dioxide. *J. Am. Chem. Soc.* **100**, 170–175 (1978).
9. Fester, J. et al. Edge reactivity and water-assisted dissociation on cobalt oxide nanoislands. *Nat. Commun.* **8**, 14169 (2017).
10. Pradigue, J. A. et al. Inverse oxide/metal catalysts in fundamental studies and practical applications: a perspective of recent developments. *J. Phys. Chem. Lett.* **7**, 2627–2639 (2016).
11. Senanayake, S. D., Stacchiola, D. & Rodriguez, J. A. Unique properties of ceria nanoparticles supported on metals: novel inverse ceria/copper catalysts for CO oxidation and the water-gas shift reaction. *Acc. Chem. Res.* **46**, 1702–1711 (2013).
12. Fu, Q. et al. Interface-confined ferrous centers for catalytic oxidation. *Science* **328**, 1141–1144 (2010).
13. Fester, J. et al. The structure of the cobalt oxide/Au catalyst interface in electrochemical water splitting. *Angew. Chem. Int. Ed.* **57**, 11893–11897 (2018).
14. Baber, A. E. et al. In situ imaging of Cu<sub>2</sub>O under reducing conditions: formation of metallic fronts by mass transfer. *J. Am. Chem. Soc.* **135**, 16781–16784 (2013).
15. Schmieder, P., Denysenko, D., Grzywa, M., Magdysyuk, O. & Volkmer, D. A structurally flexible triazolate-based metal-organic framework featuring coordinatively unsaturated copper(I) sites. *Dalton Trans.* **45**, 13853–13862 (2016).
16. Oezaslan, M., Heggen, M. & Strasser, P. Size-dependent morphology of dealloyed bimetallic catalysts: linking the nano to the macro scale. *J. Am. Chem. Soc.* **134**, 514–524 (2011).
17. Jiang, K. et al. Ordered PdCu-based nanoparticles as bifunctional oxygen-reduction and ethanol-oxidation electrocatalysts. *Angew. Chem. Int. Ed.* **55**, 9030–9035 (2016).
18. Guo, S. et al. Nanocatalyst superior to Pt for oxygen reduction reactions: the case of core/shell Ag(Au)/CuPd nanoparticles. *J. Am. Chem. Soc.* **136**, 15026–15033 (2014).
19. Strasser, P. et al. Lattice-strain control of the activity in dealloyed core–shell fuel cell catalysts. *Nat. Chem.* **2**, 454–460 (2010).
20. Koh, S. & Strasser, P. Electrocatalysis on bimetallic surfaces: modifying catalytic reactivity for oxygen reduction by voltammetric surface dealloying. *J. Am. Chem. Soc.* **129**, 12624–12625 (2007).
21. Della Pina, C., Falletta, E. & Rossi, M. Update on selective oxidation using gold. *Chem. Soc. Rev.* **41**, 350–369 (2012).
22. Zhao, G. et al. Metal/oxide interfacial effects on the selective oxidation of primary alcohols. *Nat. Commun.* **8**, 14039 (2017).
23. Zheng, X. et al. Epoxidation of propylene by molecular oxygen over unsupported AgCu<sub>x</sub> bimetallic catalyst. *Rare Met.* **34**, 477–490 (2015).
24. Huang, J. et al. The effect of the support on the surface composition of PtCu alloy nanocatalysts: In situ XPS and HS-LEIS studies. *Chin. J. Catal.* **38**, 1229–1236 (2017).
25. Friebel, D. et al. Structure, redox chemistry, and interfacial alloy formation in monolayer and multilayer Cu/Au(111) model catalysts for CO<sub>2</sub> electroreduction. *J. Phys. Chem. C* **118**, 7954–7961 (2014).
26. Zhao, L., Kong, L., Liu, C., Wang, Y. & Dai, L. AgCu/SiC-powder: a highly stable and active catalyst for gas-phase selective oxidation of alcohols. *Catal. Commun.* **98**, 1–4 (2017).
27. Liu, Q. et al. Tuning the structures of two-dimensional cuprous oxide confined on Au(111). *Nano Res.* **11**, 5957–5967 (2018).
28. Liu, Y. et al. Enhanced oxidation resistance of active nanostructures via dynamic size effect. *Nat. Commun.* **8**, 14459 (2017).
29. Monig, H. et al. Understanding scanning tunneling microscopy contrast mechanisms on metal oxides: a case study. *ACS Nano* **7**, 10233–10244 (2013).
30. Yang, F. et al. Identification of 5-7 defects in a copper oxide surface. *J. Am. Chem. Soc.* **133**, 11474–11477 (2011).
31. Fester, J. et al. Comparative analysis of cobalt oxide nanoisland stability and edge structures on three related noble metal surfaces: Au(111), Pt(111) and Ag(111). *Top. Catal.* **60**, 503–512 (2016).
32. Parker, D. H., Bartram, M. E. & Koel, B. E. Study of high coverages of atomic oxygen on the Pt(111) surface. *Surf. Sci.* **217**, 489–510 (1989).
33. Hammer, B., Morikawa, Y. & Norskov, J. K. CO chemisorption at metal surfaces and overlayers. *Phys. Rev. Lett.* **76**, 2141–2144 (1996).
34. Predel, B. *Cu-Pt (Copper-Platinum)*. (Springer, Berlin Heidelberg, 1994).
35. Kinne, M. et al. Kinetics of the CO oxidation reaction on Pt(111) studied by in situ high-resolution x-ray photoelectron spectroscopy. *J. Chem. Phys.* **120**, 7113–7122 (2004).
36. Cox, D. F. & Schulz, K. H. Interaction of CO with Cu<sup>+</sup> cations: CO adsorption on Cu<sub>2</sub>O(100). *Surf. Sci.* **249**, 138–148 (1991).
37. Su, H.-Y., Yang, M.-M., Bao, X.-H. & Li, W.-X. The effect of water on the CO oxidation on Ag(111) and Au(111) surfaces: a first-principle study. *J. Phys. Chem. C* **112**, 17303–17310 (2008).
38. Andryushechkin, B. V., Shevlyuga, V. M., Pavlova, T. V., Zhidomirov, G. M. & Eltsov, K. N. Adsorption of O<sub>2</sub> on Ag(111): evidence of local oxide formation. *Phys. Rev. Lett.* **117**, 056101 (2016).
39. Hansen, W., Bertolo, M. & Jacobi, K. Physisorption of CO on Ag(111): investigation of the monolayer and the multilayer through HREELS, ARUPS, and TDS. *Surf. Sci.* **253**, 1–12 (1991).
40. Montemore, M. M., van Spronsen, M. A., Madix, R. J. & Friend, C. M. O<sub>2</sub> activation by metal surfaces: implications for bonding and reactivity on heterogeneous catalysts. *Chem. Rev.* **118**, 2816–2862 (2018).
41. Liu, X. et al. Structural changes of Au–Cu bimetallic catalysts in CO oxidation: in situ XRD, EPR, XANES, and FT-IR characterizations. *J. Catal.* **278**, 288–296 (2011).
42. Kim, J. et al. Adsorbate-driven reactive interfacial Pt–NiO<sub>1–x</sub> nanostructure formation on the Pt<sub>3</sub>Ni(111) alloy surface. *Sci. Adv.* **4**, eaat3151 (2018).
43. Poulston, S., Parlett, P. M., Stone, P. & Bowker, M. Surface oxidation and reduction of CuO and Cu<sub>2</sub>O studied using XPS and XAES. *Surf. Interface Anal.* **24**, 811–820 (1996).
44. Hopster, H. & Ibach, H. Adsorption of CO on Pt(111) and Pt 6(111) × (111) studied by high resolution electron energy loss spectroscopy and thermal desorption spectroscopy. *Surf. Sci.* **77**, 109–117 (1978).
45. Schnadt, J. et al. Experimental and theoretical study of oxygen adsorption structures on Ag(111). *Phys. Rev. B* **80**, 075424 (2009).
46. Green, I. X., Tang, W. J., Neurock, M. & Yates, J. T. Spectroscopic observation of dual catalytic sites during oxidation of CO on a Au/TiO<sub>2</sub> catalyst. *Science* **333**, 736–739 (2011).
47. Hammer, B. & Norskov, J. K. *Theoretical Surface Science and Catalysis—Calculations and Concepts*. (Academic Press, 2000).
48. Chen, H. et al. CO and H<sub>2</sub> activation over g-ZnO layers and w-ZnO(0001). *ACS Catal.* **9**, 1373–1382 (2019).
49. Mönig, H. et al. Quantitative assessment of intermolecular interactions by atomic force microscopy imaging using copper oxide tips. *Nat. Nanotechnol.* **13**, 371–375 (2018).
50. Kresse, G. & Hafner, J. Ab initio molecular dynamics for liquid metals. *Phys. Rev. B* **47**, 558–561 (1993).
51. Hobbs, D., Kresse, G. & Hafner, J. Fully unconstrained noncollinear magnetism within the projector augmented-wave method. *Phys. Rev. B* **62**, 11556–11570 (2000).
52. Kresse, G. & Furthmüller, J. Efficient iterative schemes for ab initio total-energy calculations using a plane-wave basis set. *Phys. Rev. B* **54**, 11169–11186 (1996).
53. Perdew, J. P., Burke, K. & Ernzerhof, M. Generalized gradient approximation made simple. *Phys. Rev. Lett.* **77**, 3865–3868 (1996).
54. Henkelman, G. & Jónsson, H. Improved tangent estimate in the nudged elastic band method for finding minimum energy paths and saddle points. *J. Chem. Phys.* **113**, 9978–9985 (2000).
55. Henkelman, G., Uberuaga, B. P. & Jónsson, H. A climbing image nudged elastic band method for finding saddle points and minimum energy paths. *J. Chem. Phys.* **113**, 9901–9904 (2000).
56. Norskov, J. K. N., Studt, F., Abild-Pedersen, F. & Bligaard, T. *Fundamental Concepts in Heterogeneous Catalysis*. (Wiley, 2014).
57. Hjorth Larsen, A. et al. The atomic simulation environment—a Python library for working with atoms. *J. Phys. Condens. Matter* **29**, 273002 (2017).

## Acknowledgements

This work was financially supported by Ministry of Science and Technology of China (2017YFB0602205, 2016YFA0202803), National Natural Science Foundation of China (21972144, 91545204, 11227902), and Strategic Priority Research Program of the Chinese Academy of Sciences (XDB17020200). The authors thank Evgeny Vovk for helping with XPS measurements of powder catalysts and the support from Analytical Instrumentation Center (contract no. SPST-AIC10112914), SPST, ShanghaiTech University. Dedicated to the 70th anniversary of Dalian Institute of Chemical Physics, CAS.

### Author contributions

F.Y. and X.B. designed and supervised the project. W.H., Q.L., Ya.L., and Yu.L. carried out the STM and XPS experiments. Z.Z. and B.Y. carried out the DFT calculations. Y.W., Y.T., and D.D. carried out preparation and catalytic tests of powder catalysts. B.W., X.Z., Y.Y., and Z.L. carried out the TEM and XPS analysis of powder catalysts. F.Y., W.H., and Z.Z. prepared this manuscript.

### Competing interests

The authors declare no competing interests.

### Additional information

**Supplementary information** is available for this paper at <https://doi.org/10.1038/s41467-020-15965-8>.

**Correspondence** and requests for materials should be addressed to F.Y.

**Peer review information** *Nature Communications* thanks the anonymous reviewer(s) for their contribution to the peer review of this work.

**Reprints and permission information** is available at <http://www.nature.com/reprints>

**Publisher's note** Springer Nature remains neutral with regard to jurisdictional claims in published maps and institutional affiliations.



**Open Access** This article is licensed under a Creative Commons Attribution 4.0 International License, which permits use, sharing, adaptation, distribution and reproduction in any medium or format, as long as you give appropriate credit to the original author(s) and the source, provide a link to the Creative Commons license, and indicate if changes were made. The images or other third party material in this article are included in the article's Creative Commons license, unless indicated otherwise in a credit line to the material. If material is not included in the article's Creative Commons license and your intended use is not permitted by statutory regulation or exceeds the permitted use, you will need to obtain permission directly from the copyright holder. To view a copy of this license, visit <http://creativecommons.org/licenses/by/4.0/>.

© The Author(s) 2020